Influence of Oxygen Defects on the Structure and Magnetic Properties of $Sr_{1-x}Bi_xCoO_{3-y}$ ($0.1 \leq x \leq 0.2$) Supercell Perovskites

Christopher S. Knee,*,† Fredrik Lindberg,‡ Nasima Khan,§ Gunnar Svensson,‡ Peter Svedlindh,|| Håkan Rundlöf,⊥ Sten G. Eriksson,# and Lars Börjesson†

Departments of Applied Physics and Environmental Inorganic Chemistry, Chalmers University of Technology, SE-41296 Göteborg, Sweden, Department of Structural Chemistry, Stockholm University, SE-106 91 Stockholm, Sweden, Department of Inorganic Chemistry, Gothenburg University, SE-41296 Göteborg, Sweden, Department of Engineering Sciences, Uppsala University, Box 534, SE-751 21, Uppsala, Sweden, and Studsvik Neutron Research Laboratory, Uppsala University, SE-611 82 Nyköping, Sweden

Received November 8, 2005. Revised Manuscript Received January 9, 2006

The synthesis and structural characterization of perovskite-related $Sr_{1-x}Bi_xCoO_{3-y}$ compounds in the compositional range $0.05 \leq x \leq 0.25$ is reported. The as-prepared $x = 0.10$, 0.15, and 0.20 materials adopt *I*4/*mmm* supercell structures based on layers of CoO_6 and CoO_{6-x} oxygen-deficient layers alternating along the *c* axis. Analysis of neutron powder diffraction data reveals that the oxygen vacancies are located on two crystallographic sites in the *xy* plane, resulting in tetrahedral, square-pyramidal, and occasional octahedral cobalt environments. All three as-prepared phases are antiferromagnetically ordered at room temperature and display increasing cobalt moments with increasing Bi content, i.e., 2.14(3), 2.32(2), and 2.64(2) μ_B for $x = 0.10$, 0.15, and 0.2), respectively, at 10 K. Upon annealing under flowing oxygen, the samples undergo an exothermic phase transition to the cubic perovskite structure, indicating that the superstructure is metastable. The oxygen-annealed $x = 0.15$ sample exhibits a low-temperature spin glass phase consistent with competition between ferromagnetic and antiferromagnetic couplings. The relationship to the isostructural $Ln_{1-x}Sr_xCoO_{3-\delta}$ supercell perovskites, Ln = Y, Eu−Ho, is discussed.

Introduction

The ability of perovskite-based oxides to form stable crystal structures for a range of oxygen stoichiometries is one of the main reasons for the wide range of electronic and magnetic phenomena these materials display. The superconductivity of $YBa_2Cu_3O_{7-\delta}$[1] and the magnetoresistance displayed by $LnBaCo_2O_{5.4}$, Ln = Eu and Gd, materials[2] are just two examples of properties dependent on the presence of significant oxygen deficiencies. These compounds adopt supercell structures constructed by the regular stacking of approximate repeats units of the basic cubic perovskite unit cell, denoted a_p, i.e., $a \approx b \approx a_p$, $c \approx 3a_p$ for YBCO[3] and $a \approx a_p$, $b \approx 2a_p$, $c \approx 2a_p$ for $LnBaCo_2O_{5.4}$,[2] with the superstructures reflecting the preferential ordering of oxygen vacancies in a specific layer in the compounds. Recently, a new form of oxygen-defect-based perovskite superstructure was reported for $Sr_{0.33}Ln_{0.67}CoO_{3-\delta}$, Ln = Y, Ho, and Dy,[4] and $Y_{0.3}Sr_{0.7}CoO_{2.62}$[5] phases. The basic structure of these materials can be described by the tetragonal *I*4/*mmm* space group with unit cell given by $a \approx 2a_p$ and $c \approx 4a_p$. Analysis of neutron powder diffraction (NPD) data revealed that $Sr_{0.7}Y_{0.3}CoO_{2.62}$ consists of alternating layers of oxygen-replete CoO_6 octahedra and oxygen-deficient CoO_4 tetrahedral sheets in close similarity to the Brownmillerite $Sr_2Co_2O_5$.[6,7] However, in contrast to the chains of CoO_4 running along the 110 direction found for the Brownmillerite structure, the tetrahedra form segregated Co_4O_{12} units.[5] Furthermore, as suggested by the chemical formula $Sr_{0.7}Y_{0.3}CoO_{2.62}$, additional oxygen ions are located in the tetrahedral layers so that, locally, some of the cobalt ions adopt trigonal-bipyramidal coordinations.

Subsequently, several new studies have reported on the phase formation, structure, and magnetic properties of various $Ln_{1-x}Sr_xCoO_{3-\delta}$ ($0.05 \leq x \leq 0.5$) supercell perovskites.[8−13] NPD experiments have revealed the presence of long-range

* Corresponding author. E-mail: knee@fy.chalmers.se.
† Department of Applied Physics, Chalmers University of Technology.
‡ Stockholm University.
§ Gothenburg University.
|| Department of Engineering Sciences, Uppsala University.
⊥ Studsvik Neutron Research Laboratory, Uppsala University.
Department of Environmental Inorganic Chemistry, Chalmers University of Technology.

(1) Wu, M. K.; Ashburn, J. R.; Torng, C. J.; Hor, P. H.; Meng, R. L.; Gao, L.; Huang, Z. J.; Wang, Y. Q.; Chu, C. W. *Phys. Rev. Lett.* **1987**, *58*, 908−910.
(2) Martin, C.; Maignan, A.; Pelloquin, D.; Nguyen, N.; Raveau, B. *Appl. Phys. Lett.* **1997**, *71*, 1421.
(3) Cava, R. J.; Hewat, A. W.; Hewat, E. A.; Batlogg, B, Marezio, M.; Rabe, K. M.; Krajewski, J. J.; Peck, W. F.; Rupp, L. W. *Physica C* **1990**, *165*, 419−433.
(4) Withers, R. L.; James, M.; Goossens, D. J. *J. Solid State Chem.* **2003**, *174*, 198−208.
(5) Istomin, S. Y.; Grins, J.; Svensson, G.; Drozhzhin, O. A.; Kozhevnikov, V. L.; Antipov, E. V.; Attfield, J. P. *Chem. Mater.* **2003**, *15*, 4012−4020.
(6) Takeda, T.; Yamaguchi, Y.; Watanabe, H. *J. Phys. Soc. Jpn.* **1972**, *33*, 970.
(7) Grenier, J.-C.; Ghobane, S.; Demazeau, G.; Pouchard, M.; Hagenmuller, P. *Mater. Res. Bull.* **1979**, *14*, 831.
(8) Istomin, S. Y.; Drozhzhin, O. A.; Svensson, G.; Antipov, E. V. *Solid State Sci.* **2004**, *6*, 539−546.
(9) James, M.; Cassidy, D.; Goossens, D. J.; Withers, R. L. *J. Solid State Chem.* **2004**, *177*, 1886−1895.
(10) James, M.; Cassidy, D.; Wilson, K. F.; D. J.; Horvat, J.; Withers, R. L. *Solid State Sci.* **2004**, *6*, 655−662.

10.1021/cm052457j CCC: $33.50
Published on Web 02/09/2006

G-type antiferromagnetic (AFM) ordering for many of these phases with $T_{Néel}$ values close to room temperature.[8,11] Detailed magnetic susceptibility measurements performed on $Sr_{0.67}Y_{0.33}CoO_{2.79}$ by Goossens et al.[11] showed the coexistence of ferromagnetic domains within the long-range-ordered AFM matrix of $Sr_{0.67}Y_{0.33}CoO_{2.79}$, a feature attributed to localized compositional inhomogeneities. Meanwhile, Maignan et al.[12] recently demonstrated the extreme sensitivity of the $Sr_{2/3}Y_{1/3}CoO_{2.66+\delta}$ system to oxygen content, with a small insertion of oxygen, from $\delta = 0$ to $\delta = 0.04$, sufficient to change the material from an AFM insulator to a metallic ferromagnet. The potential for applications based on these materials is further evident from the existing interest in closely related oxygen-defect perovskites as components in solid oxide fuel cells.[14,15]

In this article, we report on the systematic investigation of $Sr_{1-x}Bi_xCoO_{3-y}$ phases with $x = 0.05-0.25$. The phase stability and electrical properties of the $Bi_{1-x}Sr_xCoO_y$ ($0.1 \leq x \leq 1.0$) series has previously been reported by Tolochko et al.,[16] and an essentially phase-pure cubic phase was identified for the composition $Bi_{0.2}Sr_{0.8}CoO_y$ from powder X-ray diffraction (PXD). Following a similar experimental procedure, we obtain perovskite-based materials for the Bi(x) compositional range $0.10 \leq x \leq 0.20$. Initial structural characterization using PXD indicated simple cubic structures. However, the presence of supercell reflections, indicative of oxygen vacancy ordering and tetragonal symmetry, is apparent from neutron and electron diffraction. Upon annealing under flowing oxygen, the structure of the materials transforms to the parent cubic ($Pm\bar{3}m$) perovskite as oxygen vacancies are filled. An accompanying change in the magnetic properties of the materials is observed. The as-prepared phases exhibit long-range antiferromagnetic order with $T_{Néel}$ values above room temperature apparent from NPD patterns. Detailed magnetization measurements for the $x = 0.15$ oxygen-annealed sample showed spin-glass behavior with frequency-dependent freezing temperatures of about 80 K. Results that are consistent with weak diffuse magnetic scattering that is seen in the neutron diffraction pattern collected at 10 K.

Experimental Section

Samples (~6 g) of $Sr_{1-x}Bi_xCoO_{3-y}$ with $x = 0.05$, 0.10, 0.15, 0.20, and 0.25 were prepared by grinding suitable amounts of $SrCO_3$, Bi_2O_3, and CoO. The reactants were initially fired at 800 °C for 20 h and then pressed into pellets and fired at 900 and 950 °C for similar lengths of time with an intermediate regrind. The samples were quenched to room temperature in air after every heat treatment. Approximately one-half of the $x = 0.15$ as-prepared sample was then heated at 900 °C for 15 h under a flow of oxygen to produce the oxygen-annealed sample. A 350 °C/h heating and cooling rate was employed. This oxygen annealing step was repeated for smaller (~1.0-g) portions of the as-prepared $x = 0.10$ and 0.20 samples.

Initial phase characterization was carried out using PXD data collected on a Siemens D5000 diffractometer (Cu K_α) radiation in the 2θ range of 20−60°. NPD data ($\lambda = 1.47$ Å) were collected for the $x = 0.10$ and 0.20 as-prepared samples at $T = 10$ K, room temperature (RT), and 500 K on the NPD instrument at Studsvik Neutron Research Laboratory, Nyköping, Sweden. Data at $T =$ RT, 400, 500, and 600 K were collected on the $x = 0.15$ as-prepared sample using the D1A diffractometer ($\lambda = 1.908$ Å) at the Institut Laue Langevin, Grenoble, France, and a further scan at 10 K was collected using the high-resolution instrument D2B with $\lambda = 1.59$ Å. Data sets at RT and 10 K were also obtained for the O_2-annealed $x = 0.15$ sample on D1A. Analysis of the nuclear and, where appropriate, magnetic structures proceeded using the Rietveld refinement program GSAS.[17]

Transmission electron microscopy (TEM) studies were performed on small amounts of finely ground samples dispersed using butanol onto a holey carbon film supported by a copper grid. The microscopes used were a JEOL JEM3010 UHR instrument operated at 300 kV for high-resolution (HRTEM) studies and a JEOL JEM2000FX instrument (200 kV) equipped with a LINK AN10000 energy-dispersive X-ray (EDX) microanalysis system for elemental analysis and electron diffraction (ED).

Magnetic measurements were performed on the as-prepared and O_2-annealed $x = 0.15$ samples in a Quantum Design MPMS-XL SQUID magnetometer. Magnetization versus temperature was studied between 5 and 300 K, following two different protocols: zero-field-cooled (ZFC) and field-cooled (FC). The ZFC magnetization was obtained by cooling the sample to 5 K in zero field, turning on a magnetic field of 50 Oe, and measuring the magnetization as the sample warmed to 300 K. The FC magnetization was subsequently obtained by measuring the magnetization, in the same applied field, as the sample cooled to 5 K. ac magnetization, $m(f) = m'(f) + im''(f)$, versus temperature was studied between 10 and 120 K for the O_2-annealed $x = 0.15$ sample. Isothermal magnetization measurements were performed by applying a large positive magnetic field (10 or 20 kOe) and measuring the magnetization as a function of decreasing field. Because the experimental results gave indications of magnetic irreversibility, the field sweep was continued to negative fields until the magnetization changed sign.

To monitor the oxygen uptake of the samples, thermal analysis in O_2 was performed in a LABSYS SETARAM apparatus up to 900 °C with a temperature ramp of 5 °C/min. Iodometric titrations were also done for the as-prepared samples with $x = 0.10$ and 0.20 and the O_2-annealed $x = 0.15$ sample. About 50 mg of the sample was dissolved in an acidic 20% solution of KI, and the excess iodine was back-titrated with $Na_2S_2O_3$ with starch added as an indicator.

Results

Phase Formation. Figure 1a shows the PXD scans obtained for the $0.05 \leq x \leq 0.25$ as-prepared samples. For $x = 0.10$, 0.15, and 0.20, patterns consistent with pure cubic ($Pm\bar{3}m$), perovskite samples were obtained. In addition to the perovskite phase, the $x = 0.05$ sample contained a significant level of the rhombohedral phase $Sr_6Co_5O_{15}$[18] (marked by the asterisks in the figure) estimated to be ~35% from the relative intensities of the main reflections. For the

(11) Goossens, D. J.; Wilson, K. F.; James, M.; Studer, A. J.; Wang, X. L. *Phys. Rev. B* **2004**, *69*, 134411.
(12) Maignan, A.; Hebert, S.; Caignaert, V.; Pralong, V.; Pelloquin, D. *J. Solid State Chem.* **2005**, *178*, 868−873.
(13) Goossens, D. J.; Wilson, K. F.; James, M. J. *Phys. Chem. Solids* **2005**, *66*, 169−175.
(14) Adler, S. B. *Solid State Ionics* **1998**, *111*, 125.
(15) Skinner, S. J. *Int. J. Inorg. Mater.* **2001**, *3*, 113.
(16) Tolochko, S. P.; Kononyuk, I. F.; Ivashkevich, L. S.; Lyakhov, A. *Inorg. Mater.* **1993**, *29*, 1375−1379.
(17) Larson, A. C.; von Dreele, R. B. *General Structure Analysis System*; Los Alamos National Laboratories: Los Alamos, NM, 1994.
(18) Harrison, W. T. A.; Hegwood, S. L.; Jacobson, A. J. *J. Chem. Soc., Chem. Commun.* **1995**, 1953−1954.

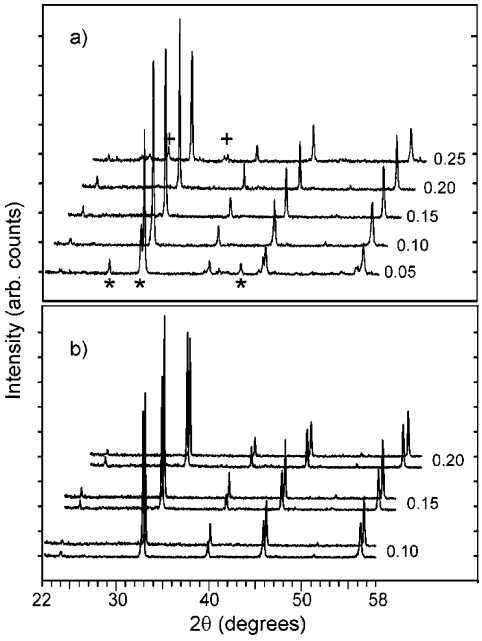

Figure 1. (a) PXD patterns obtained for the $Sr_{1-x}Bi_xCoO_{3-y}$ $0.05 \leq x \leq 0.25$ series. Reflections from the impurity phases $Sr_6Co_5O_{15}$ and $Bi_2Sr_2Co_3O_y$ are marked by * and +, respectively. (b) PXD patterns of the oxygen-annealed samples shown above the scans obtained for their as-prepared precursors.

$x = 0.25$ sample, the cubic phase was also observed to be accompanied by the impurity phase $Bi_2Sr_3Co_2O_y$,[19] indicating that the limit of Bi solubility into the perovskite structure had been reached.[16] The only evidence of a possible symmetry lower than cubic was a weak shoulder on the most intense (110) perovskite reflection at $2\theta \approx 32.5$ ° for the as-prepared $Sr_{0.9}Bi_{0.1}CoO_{3-y}$ sample. The PXD patterns obtained for the $x = 0.10$, 0.15, and 0.20 O_2-annealed samples, vertically displaced from the scans of their as-prepared counterparts, are shown in Figure 1b. A significant shift to higher 2θ values is apparent for the O_2-annealed samples, indicating a contraction of the unit cell consistent with oxidation of cobalt. The peak widths of the O_2-annealed samples were also seen to be reduced in comparison with their as-prepared counterparts. The cubic cell parameters for the as-prepared and O_2-annealed samples, refined from the PXD data using the CELREF program,[20] are plotted in Figure 2. The as-prepared samples do not follow the expected trend of a reduction in cell parameter as the Sr^{2+} is replaced by the smaller Bi^{3+} ion but instead show an expansion of ~0.025 Å across the series. The O_2-annealed samples reflect the trend established for the as-prepared materials, with the $x = 0.20$ sample showing the greatest contraction after oxidation.

Neutron Diffraction Refinements. In contrast to the PXD data, the neutron diffraction patterns obtained for the three as-prepared samples revealed several reflections that could not be indexed using a simple cubic unit cell. From

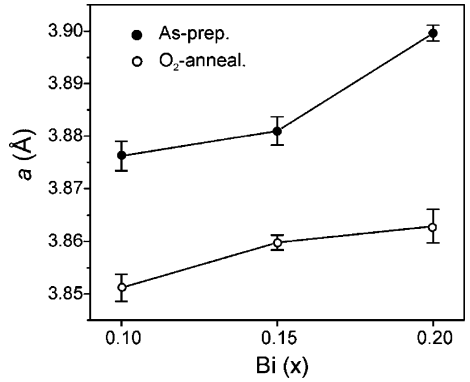

Figure 2. Comparison of the cubic cell parameter, *a*, for as-prepared and O_2-annealed samples.

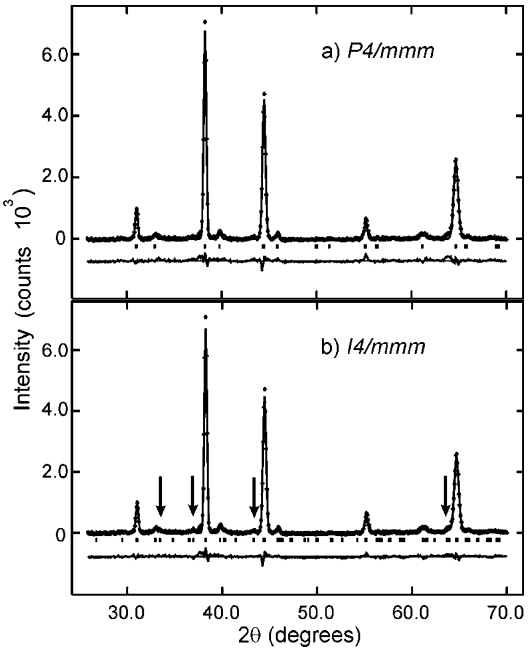

Figure 3. Comparison of the agreement achieved to the 500 K NPD pattern of $Bi_{0.1}Sr_{0.9}CoO_{3-y}$ using the (a) *P*4/*mmm* and (b) *I*4/*mmm* structural models.

comparison with related phases in the $Sr_{1-x}Ln_xCoO_{3-\delta}$ series, tetragonal *P*4/*mmm* ($a \approx a_p$, $c \approx 2a_p$)[10] and *I*4/*mmm* ($a \approx 2a_p$, $c \approx 4a_p$)[4,5] structural models were tested and found to provide good fits to the observed data. Significant extra intensity was also apparent for some supercell peaks in the 10−60° 2θ range of the RT patterns, indicating long-range antiferromagnetic ordering of the cobalt spins. To satisfactorily differentiate between the *P*4/*mmm* and *I*4/*mmm* structural descriptions, the 500 K data sets, which had no magnetic contribution to the low-2θ reflections, were analyzed. Figure 3 shows that several weak peaks observed for $Sr_{0.9}Bi_{0.1}CoO_{3-y}$ that are not included in the *P*4/*mmm* model are fitted using the *I*4/*mmm* structural description. The improved agreement between the observed and calculated profiles is also reflected in the reduced refinement statistics obtained for the *I*4/*mmm* analysis, i.e., $\chi^2 = 2.42$, $R_{wp} = 7.00\%$, $R_p = 5.28\%$ for *P*4/*mmm* (25 variables) and $\chi^2 = 2.11$, $R_{wp} = 6.57\%$, $R_p = 5.01\%$ (32 variables) for *I*4/*mmm*. A similar preference for the larger supercell was obtained for the other as-prepared compositions. In the latter stages of the refinements, oxygen ion occupancies were refined. In particular, the 8i (0, *y*, 0) and 8j (*x*, $^1/_2$, 0) positions favored

(19) Tarascon, J.-M.; Ramesh, R.; Barboux, P.; Hedge, M. S.; Hull, G. W.; Greene, L. H.; Giroud, M.; Lepage, Y.; Mckinnon, W. R.; Waszcak, J. V.; Schneemeyer, L. F. *Solid State Commun.* **1989**, *71*, 663−668.

(20) Laugier, J.; Bochu, B. *CELREF*, version 3; Laboratoire des Materiaux et du Génie Physique de l'Ecole Supérieure de Physique de Grenoble, Grenoble, France, 2002.

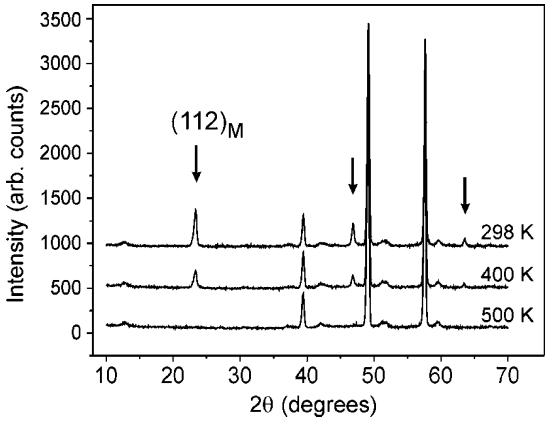

Figure 4. Decay of the magnetic reflections observed for as-prepared $Bi_{0.15}Sr_{0.85}CoO_{3-y}$ using D1A ($\lambda = 1.909$ Å).

a redistribution from the starting model adopted from the neutron refinement of $Sr_{0.7}Y_{0.3}CoO_{2.62}$.[5] The thermal parameters of the sites were first constrained to be equal before their occupancies were allowed to vary independently, and the 8i site was found to favor a reduction from full occupancy whereas the 8j position refined to approximately 50% occupancy. The position of the oxygen 8j ions refined to $x \approx 0.27$ for all three phases, significantly different from the starting value of 0.399.[5] The strong correlation for the three A-sites in the structure also necessitated the use of a constrained thermal parameter in the analyses. Probably as a result of this correlation, the contrast between the scattering lengths of Sr and Bi proved insufficient to reliably refine a location for the Bi ions. The sites were therefore modeled with the scattering length adjusted to an average of the scattering expected for Sr($1 - x$) and Bi(x).

Additional magnetic Bragg intensity was apparent in the NPD patterns collected for the as-prepared samples in all data sets collected below 500 K. In particular, the intensity of the (112) nuclear reflection at $2\theta \approx 23.5°$ is negligible; however, it coincides with the most intense magnetic peak as shown in Figure 4 for $Sr_{0.85}Bi_{0.15}CoO_{3-y}$. This behavior is similar to that reported for $Sr_{0.7}Dy_{0.3}CoO_{2.62}$,[8] and the magnetic intensity was fitted using the same G-type antiferromagnetic structure with neighboring cobalt spins aligned in a collinear fashion parallel and antiparallel with the c axis. The magnetic form factor of cobalt +3 was used, and the magnetic space group $I4/mm'm$ described the spins. The moments for Co(1) and Co(2) were constrained to be equal during the refinements, and values of 2.64(2), 2.32(2), and 2.14(3) μ_B were obtained for the $x = 0.20$, 0.15, and 0.10 samples, respectively, at $T = 10$ K. The low-temperature data sets for the $x = 0.10$ and 0.20 samples also revealed unexplained intensity at a d-spacing of ~4.9 Å that was identified as the (111) magnetic reflection of CoO ($T_{Néel} \approx 290$ K).[21] For the $x = 0.10$ sample, this magnetic intensity was too weak to be meaningfully fitted, allowing an upper limit of ≤0.5 wt % of CoO to be estimated. For the $x = 0.20$ sample, the peak was significantly more intense; the data sets collected at ambient and 500 K were therefore reexamined, and weak nuclear reflections from CoO were detected. The atomic and magnetic contributions from CoO[21] were therefore included in the refinements, and a weight percentage of 2.2(4)% was determined. The agreement achieved between the 10 K data and the calculated profiles for the $Sr_{0.8}Bi_{0.2}CoO_{3-y}$ refinement is shown in Figure 5.

(21) Roth, W. L. *Phys. Rev.* **1958**, *110*, 1333.

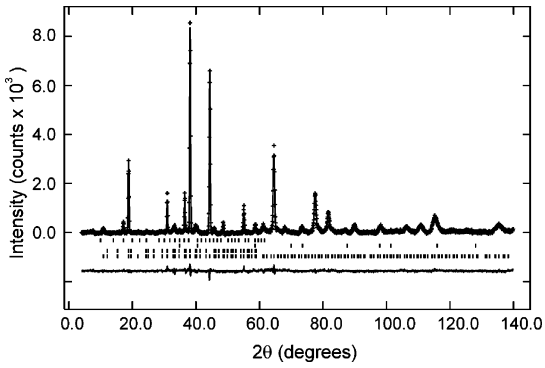

Figure 5. NPD pattern obtained for as-prepared $Bi_{0.20}Sr_{0.80}CoO_{3-y}$ at 10 K on the NPD instrument ($\lambda = 1.47$ Å). Crosses are observed data, and lines are calculated and difference plots. Reading from bottom to top, vertical tick marks indicate the positions of allowed reflections for the nuclear structure of $Bi_{0.20}Sr_{0.80}CoO_{3-y}$, its magnetic structure, and the nuclear and magnetic structures of CoO.

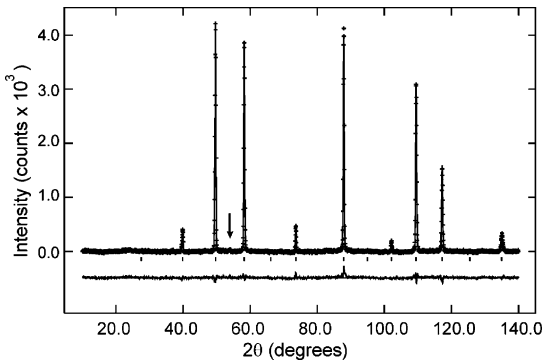

Figure 6. NPD pattern obtained for O_2-annealed $Bi_{0.15}Sr_{0.85}CoO_{3-y}$ at 10 K on D1A ($\lambda = 1.909$ Å). The plot follows the same labeling style as in Figure 5. A weak reflection from the vanadium sample holder at $2\theta \approx 53°$ is marked.

Inspection of the NPD patterns obtained for the oxygen-annealed $Sr_{0.85}Bi_{0.15}CoO_{3-y}$ sample showed that the supercell reflections were missing and the structure of the phase was satisfactorily described as a simple cubic $Pm\bar{3}m$ perovskite. Refinement of the oxygen occupancy gave a small reduction to approximately 0.90 and an accompanying improvement in the quality of fit. No coherent magnetic Bragg reflections were apparent in either the RT or 10 K data. The agreement achieved for the 10 K Rietveld analysis is presented in Figure 6. Tables 1 and 2 summarize the refined crystallographic and magnetic parameters for the as-prepared materials and O_2-annealed $x = 0.15$ sample, respectively. Derived bond distances and bond angles are reported in Tables 3 and 4.

Electron Diffraction and HRTEM. Selected-area electron diffraction patterns recorded for as-prepared $Sr_{1-x}Bi_xCoO_{3-y}$, $x = 0.10$, 0.15, and 0.20, confirmed the presence of a superstructure of the parent cubic perovskite structure for all samples. The electron diffraction (ED) patterns could not be uniquely indexed as single-zone-axis patterns because of microtwinning in the crystallites, a phenomenon commonly observed for these types of materials.[22,23] A representative example of such a pattern found for the $x = 0.20$ sample is shown in Figure 7a. The pattern

Table 1. Refined Atomic and Magnetic Parameters for As-Prepared $Sr_{1-x}Bi_xCoO_{3-y}$, $x = 0.10$, 0.15, and 0.20, Samples from NPD Data Collected at RT[a]

			$Bi_{1-x}Sr_xCoO_{3-y}$		
atom	site	variables	0.10	0.15	0.20
Sr/Bi(1)	4e (0, 0, *z*)	*z*	0.8681(10)	0.8676(8)	0.8669(10)
		B_{iso} (Å^2)	1.20(8)	1.37(5)	1.65(9)
Sr/Bi(2)	8g (0, $^1/_2$, *z*)	*z*	0.8713(7)	0.8707(4)	0.8710(6)
		B_{iso} (Å^2)	1.20(8)	1.37(5)	1.65(9)
Sr/Bi(3)	4e (0, 0, *z*)	*z*	0.3606(10)	0.3640(8)	0.3626(10)
		B_{iso} (Å^2)	1.20(8)	1.37(5)	1.65(9)
Co(1)	8h (*x*, *x*, 0)	*x*	0.757(2)	0.740(1)	0.749(2)
		B_{iso} (Å^2)	0.75(12)	0.25(1)	1.15(12)
Co(2)	8f ($^1/_4$, $^1/_4$, $^1/_4$)	B_{iso} (Å^2)	0.75(12)	0.25(1)	1.15(12)
O(1)	16n (0, *y*, *z*)	*y*	0.2484(11)	0.2543(10)	0.2536(13)
		z	0.2439(7)	0.2447(6)	0.2431(7)
		B_{iso} (Å^2)	0.61(9)	1.57(11)	1.63(12)
O(2)	16m (*x*, *x*, *z*)	*x*	0.2702(9)	0.2634(9)	0.2730(11)
		z	0.1155(4)	0.1190(3)	0.1152(5)
		B_{iso} (Å^2)	2.6(2)	3.1(3)	3.8(3)
O(3)	8i (0, *y*, 0)	*y*	0.765(3)	0.779(2)	0.784(3)
		B_{iso} (Å^2)	2.3(3)	2.3(3)	2.9(3)
		occ	0.79(3)	0.77(2)	0.73(3)
O(4)	8j (*x*, $^1/_2$ 0)	*x*	0.286(4)	0.261(3)	0.273(4)
		B_{iso} (Å^2)	2.3(3)	2.3(3)	2.9(3)
		occ	0.48(3)	0.59(2)	0.55(3)
	a (Å)		7.7322(5)	7.78412(3)	7.7978(9)
	c (Å)		15.528(2)	15.5886(10)	15.618(3)
	V (Å^3)		928.4(1)	944.56(8)	949.7(2)
	μ_{AFM} (μ_B)[b]		1.46(4)	2.08(2)	2.28(3)
	χ^2		2.91	3.41	2.52
	R_{wp} (%)		6.51	6.59	6.25
	R_p (%)		4.88	5.12	4.87

[a] Space group *I*4/*mmm*. [b] Co(1) μ_{AFM} constrained to equal Co(2) μ_{AFM}.

Table 2. Refined Atomic Parameters for O_2-Annealed $Sr_{0.85}Bi_{0.15}CoO_{3-y}$ from NPD Data Collected at RT and 10 K[a]

atom	site	variable	RT	10 K
Sr/Bi	1b ($^1/_2$, $^1/_2$, $^1/_2$)	B_{iso} (Å^2)	1.40(5)	1.48(5)
		occ	0.88(5)/0.12(5)	0.855(4)/0.145(4)
Co	1a (0, 0, 0)	B_{iso} (Å^2)	0.58(9)	0.32(7)
O(1)	3d (0, 0, $^1/_2$)	B_{iso} (Å^2)	1.82(4)	1.61(4)
		occ	0.908(8)	0.912(6)
	a (Å)		3.86216(7)	3.85340(6)
	V (Å^3)		57.609(2)	57.2178(2)
	χ^2		2.94	2.74
	R_{wp} (%)		5.54	3.97
	R_p (%)		4.48	2.91

[a] Space group $Pm\bar{3}m$.

Table 3. Derived Interatomic Distances (Å) and Selected Cobalt−Oxygen Bond Angles (deg) of As-Prepared $Bi_{1-x}Sr_xCoO_{3-y}$ Compounds at RT

	0.10	0.15	0.20
Co(1)−O(2) × 2	1.819(8)	1.857(5)	1.816(8)
Co(1)−O(3) × 2[a]	1.877(17)	2.037(14)	1.974(20)
Co(1)−O(4) × 2[b]	2.018(21)	1.876(12)	1.951(19)
Co(2)−O(1) × 4	1.9354(5)	1.9479(4)	1.9526(7)
Co(2)−O(2) × 2	2.101(7)	2.048(6)	2.120(8)
Sr(1)−O(1) × 4	2.591(15)	2.638(12)	2.619(17)
Sr(1)−O(2) × 4	2.966(10)	2.919(11)	3.024(12)
Sr(1)−O(3) × 4[a]	2.739(19)	2.700(15)	2.676(21)
Sr(2)−O(1) × 2	2.642(13)	2.630(10)	2.620(14)
Sr(2)−O(1) × 2	2.774(12)	2.740(10)	2.772(14)
Sr(2)−O(2) × 4	2.7504(12)	2.740(10)	2.7770(15)
Sr(2)−O(3) × 2[a]	2.861(16)	2.957(13)	2.994(18)
Sr(2)−O(4) × 2[b]	2.980(27)	2.865(18)	2.930(27)
Sr(3)−O(1) × 4	2.641(16)	2.717(12)	2.719(17
Sr(3)−O(2) × 4	2.540(10)	2.606(11)	2.527(12)
Sr(3)−O(4) × 4[b]	2.73(3)	2.81(2)	2.78(3)
O(3)−Co(1)−O(4)[a,b]	172(1)	173(1)	177(1)
O(1)−Co(2)−O(1)	174.3(6)	175.0(5)	173.5(6)

[a] O(3) site is at approximately 70% occupation. [b] O(4) site is at approximately 50% occupation.

can be indexed with a superimposition of three different zone-axis patterns of a superstructure of perovskite $\langle 100 \rangle_p$ with an I-centered tetragonal space group having unit cell axes of $a \approx 2a_p$ and $c \approx 4a_p$ (namely, [100], [010], and [001], with [100] and [010] at right angles to each other), supporting the validity of the *I*4/*mmm* structure determined by NPD. The close structural relation to the supercell adopted by the $Sr_{1-x}Ln_xCoO_{3-\delta}$ (Ln = Y, Eu−Ho; $x \approx 0.3$) materials[4,5,8] is further emphasized by the simulated ED patterns of three superimposed zone-axis patterns shown in Figure 7b. (The structure of $Sr_{0.7}Y_{0.3}CoO_{2.62}$ was used as the model.) The HRTEM micrographs also support this finding, with a tetragonal supercell and microtwinning of differently ordered domains apparent in Figure 8. Fast Fourier transforms (FFTs) of various areas of the HRTEM micrographs confirm the varying orientations of the different domains. Figure 9 shows the HRTEM image and ED pattern recorded from the $x = 0.20$ O_2-annealed sample and reveals that the long-range vacancy ordering is lost—an observation repeated for the other oxygen-treated samples. In addition to the spots coming from the perovskite substructure, only diffuse or streaked reflections are seen in the ED patterns, indicating that some local ordering of vacancies and A cations still remains. Finally, EDX measurements were carried out on a representative number of crystallites, for both as-prepared

(22) Lindberg, F.; Svensson, G.; Istomin, S. Y.; Aleshinskaya, S. V.; Antipov, E. V. *J. Solid State Chem.* **2004**, *1592*, 177.
(23) Nakayama, N.; Takano, M.; Inamura, S.; Nakanishi, N.; Kosuge, K. *J. Solid State Chem.* **1987**, *71*, 403.

Table 4. Derived Interatomic Distances (Å) of O_2-Annealed $Bi_{1-x}Sr_xCoO_{3-y}$ Compounds

distances	0.10[a]	0.15[b]	0.20[a]
Co−O × 6[c]	1.926(2)	1.93108(4) 1.92670(3)	1.931(2)
Sr/Bi−O × 12[c]	2.723(3)	2.73096(4) 2.72477(3)	2.731(3)

[a] Determined from RT PXD cell parameter. [b] For the $x = 0.15$ sample, the upper (lower) values are from NPD data collected at RT (10 K). [c] O site is at approximately 91% occupation.

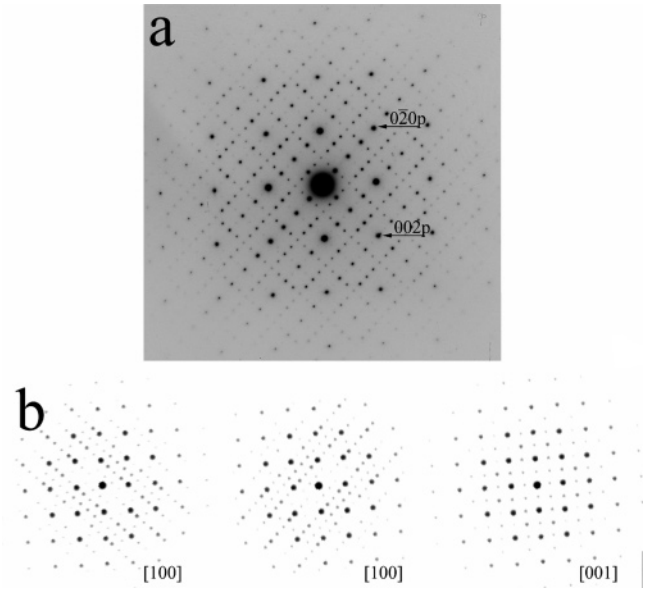

Figure 7. (a) ED pattern taken along the ⟨100⟩ axis of the perovskite subcell of as-prepared $Sr_{0.8}Bi_{0.2}CoO_{3-y}$. The pattern can be explained by a tetragonal unit cell with axes $a \approx 2a_p$ and $c \approx 4a_p$ with microtwinning of domains oriented along three different supercell zone axes as indicated in (b).

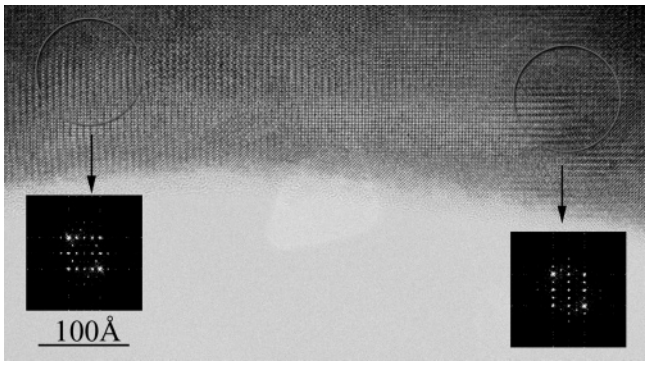

Figure 8. HREM micrograph recorded along the same zone axis as in Figure 7. FFTs calculated for different domains indicate microtwinning.

and O_2-annealed samples, and these confirmed the targeted stoichiometry of the heavier elements.

Thermal Analysis. Figure 10 shows the thermogravimetric and calorimetric responses of the as-prepared $x = 0.10$ and 0.20 samples upon heating under a flow of oxygen. The samples both exhibit increases in mass consistent with significant uptake of oxygen. Incorporation of oxygen is accompanied by endothermic decreases in the heat flow, as expected. The heat flow traces show sharp exothermic peaks at 660 and 710 °C for the 0.10 and 0.20 samples, respectively, that we attribute to the structural phase transition from the tetragonal supercell to the cubic perovskite structure. The endotherms at higher temperatures (∼870 °C) suggest partial

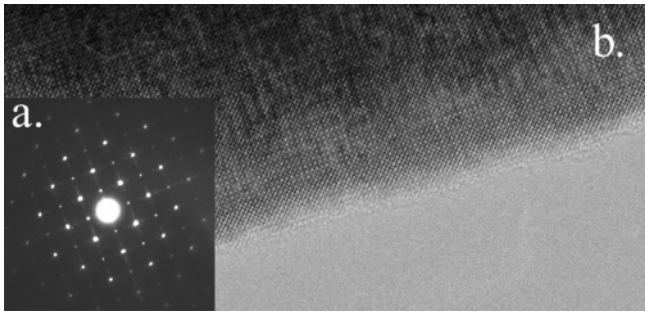

Figure 9. (a) ED pattern and (b) HREM micrograph of the O_2-annealed $x = 0.2$ sample. The superstructure reflections are absent. Diffuse scattering in the ED pattern probably indicates partial ordering of some remaining oxygen vacancies.

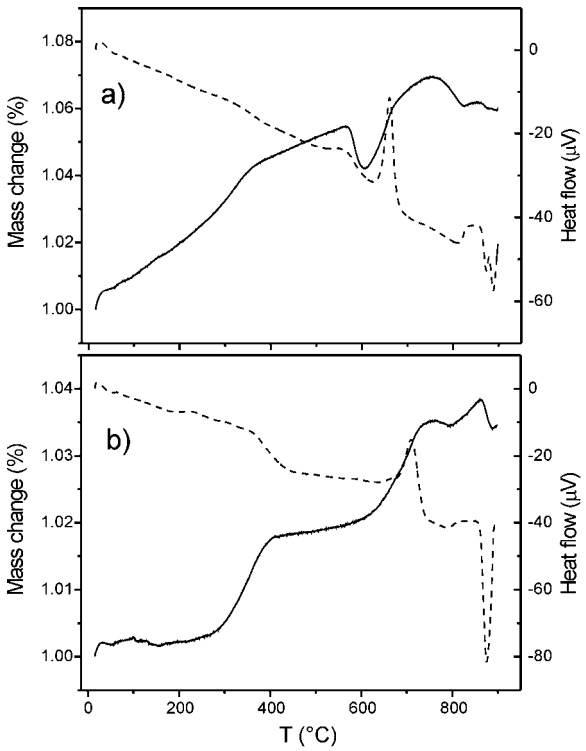

Figure 10. TGA (solid line) and calorimetric (broken line) scans obtained for the as-prepared (a) $x = 0.10$ and (b) 0.20 samples while being heated under flowing oxygen.

melting of the sample. PXD revealed traces of Bi_2O_3 in the remains after the experiments that might have been released from the sample because of this. From the iodometric titrations, oxygen contents of $O_{2.73(3)}$, $O_{2.72(2)}$, and $O_{2.60(4)}$ were obtained for the $x = 0.10$, 0.15, and 0.20 as-prepared phases, respectively. Analysis of the oxygenated $x = 0.15$ sample yielded $O_{2.90(1)}$.

Magnetization Study. Figure 11 shows the temperature dependence of the ZFC and FC magnetizations for the as-prepared and O_2-annealed $x = 0.15$ samples. The magnetization versus applied field results at various temperatures are plotted in Figure 12a,b. The magnetic behavior of the samples is clearly very different. The magnetization of the as-prepared sample is much smaller (by ∼2 orders of magnitude) than that of the O_2-annealed phase and shows very little variation with temperature upon cooling from RT—behavior that indicates the presence of dominant antiferromagnetic coupling and that is consistent with the presence of AFM Bragg reflections in the RT NPD pattern. A very small irreversibility

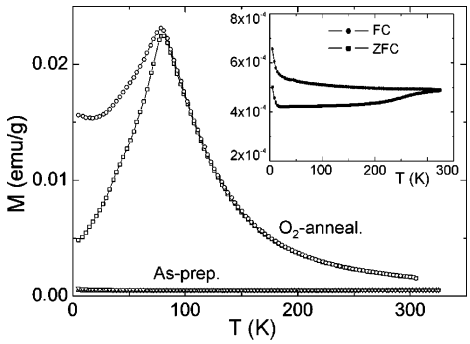

Figure 11. Temperature dependence of the magnetization of as-prepared and O_2-annealed $Sr_{0.85}Bi_{0.15}CoO_{3-y}$ in an applied field of 50 Oe. Inset shows the behavior of the as-prepared sample at an enlarged scale.

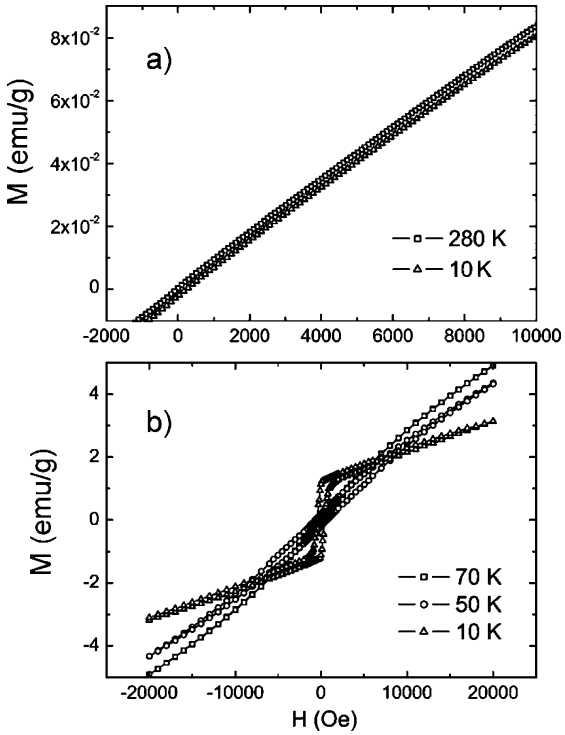

Figure 12. Magnetization as a function of applied field for (a) as-prepared and (b) O_2-annealed $Sr_{0.85}Bi_{0.15}CoO_{3-y}$ at various temperatures.

is visible (inset of Figure 11) that might be due to some weak tendency for spontaneous phase separation or a spin-canted magnetic ground state for which we find no evidence from our NPD analyses.

The significantly enhanced magnetization for the O_2-annealed sample is, to some degree, reminiscent of the effect observed for the oxygenated $Sr_{2/3}Y_{1/3}CoO_{2.66+\delta}$, $\delta = 0.04$, sample reported by Maignan et al.[12] and suggests an increasing influence of ferromagnetic couplings in this material. The observed behavior is not that of ferro- or ferrimagnetic materials but rather resembles that of a spin glass material with magnetic irreversibility developing, as evidenced by the divergence between the FC and ZFC magnetization curves at temperatures below the cusp of the $M(T)$ curves. The $M(H)$ curves shown in Figure 12b further emphasize the complexity of the O_2-annealed sample; these curves show a magnetic hysteresis at temperatures below the cusp temperature and for low applied magnetic fields, whereas for sufficiently large fields, the magnetic response exhibits an almost linear increase with increasing field. The

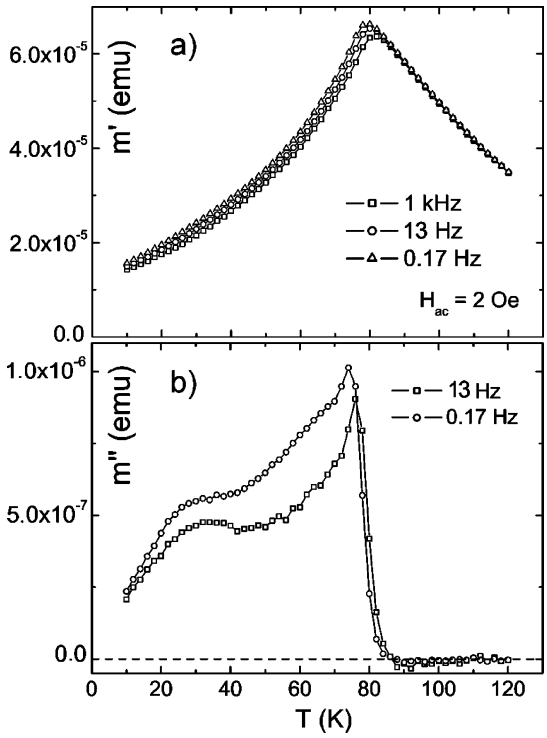

Figure 13. Frequency dependence of the (a) real m' and (b) imaginary m'' components of the ac magnetization of the O_2-annealed sample.

high-field behavior is not archetypical to spin-glass materials, which suggests that, although the sample exhibits competing FM and AFM interactions, it is the AFM couplings that dominate. At low temperatures, $T \leq 40$ K, the hysteresis curves appear to consist of two parts, one being similar to that observed at higher temperatures and one being more ferro- or ferrimagnetic-like, suggesting the presence of a magnetically active impurity. ac susceptibility versus temperature measurements were carried out for different frequencies of the ac magnetic field ($f = 0.17$ Hz, 13 Hz, and 1 kHz), and the results are shown in Figure 13. The presence of a cusp in $m'(T)$ at a frequency-dependent temperature (Figure 13a), closely coinciding with an inflection point in $m''(T)$ (Figure 13b), strongly reinforces the impression of a spin-glass state.

Discussion

The synthesis and initial structural characterization of the $Sr_{1-x}Bi_xCoO_{3-y}$, $0.05 \leq x \leq 0.25$, series using PXD revealed three apparently cubic perovskite phases for $x = 0.10$, 0.15, and 0.20. As reported by Tolochko et al.,[16] stabilization of the $Bi_2Sr_3Co_2O_y$ phase became more favorable when the Bi^{3+} content was increased above $x = 0.20$. The tendency for the samples to melt upon heating above 900 °C also increased with levels of Bi >0.20. For compositions with $x < 0.10$, the concentration of Bi appears to be too small to stabilize a perovskite-based structure, and $Sr_6Co_5O_{15}$ was also obtained. The importance of quenching the phases was underlined when PXD patterns of samples that were allowed to furnace cool revealed $Sr_6Co_5O_{15}$ as the major phase, an observation also reported by Tolochko et al. for $Bi_{0.2}Sr_{0.8}CoO_y$. No sign of melting was recorded during the preparation of the oxygen-annealed samples. Possibly, the

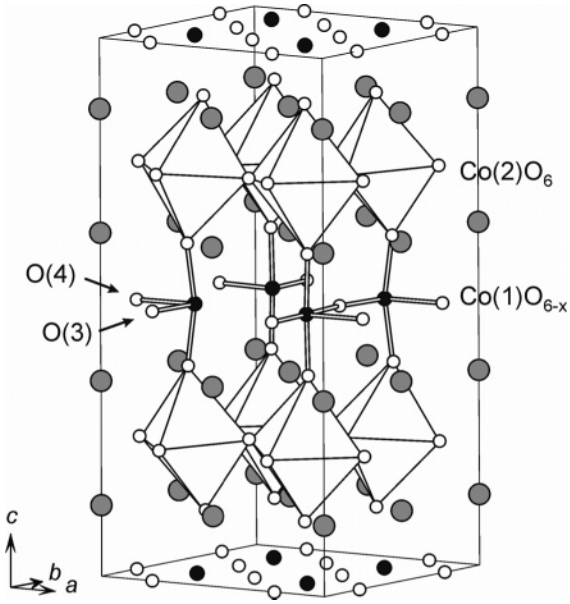

Figure 14. Crystal structure of the as-prepared $Sr_{1-x}Bi_xCoO_{3-y}$ materials. Large shaded circles represent Sr/Bi ions, small open circles are oxygen ions, and small filled circles are Co(1) positions. Bonding between the Co(1) ions and surrounding O(3) and O(4) oxygen sites is shown for the middle layer.

partial melting of the TGA samples reflects the smaller sample sizes. Alternatively, it might be linked to the specific experimental conditions, e.g., temperature, oxygen flow rate, etc. experienced by the samples.

The greater sensitivity of neutron diffraction to oxygen revealed that the as-prepared phases, $Bi_{0.10}Sr_{0.90}CoO_{3-y}$, $Bi_{0.15}Sr_{0.85}CoO_{3-y}$, and $Bi_{0.20}Sr_{0.80}CoO_{3-y}$, in fact adopt *I*4/*mmm* supercell structures based on alternate stacking of oxygen-replete and -deficient layers. The crystal structure of the $Sr_{1-x}Bi_xCoO_{3-y}$, $0.10 \leq x \leq 0.20$, phases is shown in Figure 14. In addition to the oxygen-deficient $Co(1)O_{4-x}$ layers, the materials display correlated rotations of the $Co(2)O_6$ octahedra that necessitate the quadrupling of the perovskite subcell along the *c* direction. It should be noted that the as-prepared materials, in common with the $Sr_{1-x}Ln_xCoO_{3-\delta}$ phases, are very close to being cubic. The level of tetragonal distortion (as defined by the ratio $2a/c$) at RT is highest for the $x = 0.10$ sample at 1.0028 and is approximately 1.0015 for both the $x = 0.15$ and 0.20 samples, which explains the absence of clear peak splitting in our PXD data. The level of vacancy ordering in the oxygen-deficient $Co(1)O_{4-x}$ layers of the $Sr_{1-x}Bi_xCoO_{3-y}$ phases is less perfect than that found in the parent compound $Sr_{0.7}Y_{0.3}CoO_{2.62}$. This is apparent from the structural refinements, which show deficiency at the O(3) site and an increased occupation of the O(4) site. Trail refinements confirm that this change in oxygen distribution on the 8i and 8j oxygen sites results in the significantly weaker intensity of the supercell reflections apparent for the Bi-containing phases. The structural analysis also revealed a significant shift of the O(4) oxygen along the *x* direction toward a position between neighboring cobalt ions. Consequently, the environment of the Co(1) ion is most accurately described as a distorted square pyramid when both O(3) sites are occupied and an O(4) is also present. This is an arrangement closer to that reported for $Sr_{0.33}Ln_{0.67}CoO_{3-\delta}$, Ln = Y, Ho, and Dy,[4] than the trigonal-bipyramidal coordination found for $Sr_{0.7}Y_{0.3}CoO_{2.62}$.[5]

For the $Sr_{1-x}Ln_xCoO_{3-\delta}$ phases, Ln = Y, Eu−Ho, the $a \approx 2a_p$, $c \approx 4a_p$ supercell is obtained for $x \geq 0.20$.[8] Stabilization of the superstructure is believed to be linked to ordering of the lanthanide site on the Sr(3) site, which, in turn, is argued to favor ordering of the oxygen vacancies into an oxygen-deficient $Co(1)O_{4-x}$ layer. In the present case, the difference between the ionic radii of Sr^{2+} and Bi^{3+} is significantly reduced in comparison to the largest lanthanide, i.e., Eu^{3+}, for which the tetragonal supercell has been reported.[8] Hence, the likelihood of A-site ordering based solely on size arguments would be expected to diminish greatly when trivalent Ln ions are replaced by Bi^{3+}. Instead, our results suggest that stabilization of the structure type might occur on the basis of A-site ordering due to charge effects. The similar scattering lengths of Bi and Sr, and the associated strong correlation effects, mean that it is not possible to draw any firm conclusions about A-cation ordering from Rietveld analysis of the NPD data. However, bond valence sum (BVS) calculations[24] for the Sr/Bi(3)−O distances of the as-prepared phases, using the RT oxygen occupancy factors and bond lengths (Tables 1 and 3), indicate that occupancy of the site by bismuth is favored. The calculated BVS for this position is +2.6 and +2.4 for the $x = 0.10$ and 0.20 compositions, respectively. The presence of a mixed cobalt valence state in the $Sr_{1-x}Bi_xCoO_{3-y}$ phases also means that the possibility of B-site charge ordering as a source for the supercell formation must be considered. Structural transitions in closely related perovskite-based $LnBaCo_2O_5$ (Ln = Tb, Dy, Ho) systems due to ordering of Co^{2+} and Co^{3+} have been reported,[25] although, so far, little direct evidence of charge ordering in the $Sr_{1-x}Ln_xCoO_{3-\delta}$ supercell materials has emerged. BVS calculations for the $Sr_{1-x}Bi_xCoO_{3-y}$ series give the best agreement if Co(III) is assumed at both sites, with a BVS close to +2.9 for the Co(2) octahedra and slightly lower values obtained for Co(1).

The cell parameters obtained for as-prepared $Sr_{1-x}Bi_xCoO_{3-y}$ are larger than those obtained for the $Sr_{1-x}Ln_xCoO_{3-\delta}$ supercell systems, consistent with both the increased size of Bi^{3+} and the lower level of substitution. The materials show isotropic thermal contraction on cooling, as expected for pseudocubic systems (Figure 15). The increasing size of the cell parameters with increasing *x*, however, runs contrary to the anticipated trend for substitution of smaller Bi^{3+} onto the A sites. A comparison of the ionic radii expected for Sr^{2+} and Bi^{3+} ions in 9-fold coordination reveals a value of ~1.24 Å for Bi^{3+} when its lone pair is active[26] and 1.31 Å for Sr^{2+}.[27] If the lone-pair character is not dominant, the ionic radius of Bi^{3+} decreases to ~1.16 Å.[27] To explain the cell parameter behavior, the level of oxygen deficiency in the samples, as well as the corresponding cobalt oxidation states, must be considered. From the results of the iodometric titrations, we obtain a trend of lowering cobalt oxidation state

(24) Brese, N. E.; O'Keeffe, M. *Acta Crystallogr.* **1991**, *B47*, 192.
(25) Fauth, F.; Suard, E.; Caignaert, V.; Domenges, B.; Mirebeau, I.; Keller, L. *Eur. Phys. J. B* **2001**, *21*, 163−174. was 21
(26) Shannon, R. D.; Prewitt, C. T. *Acta Crystallogr.* **1969**, *B25*, 925.
(27) Shannon, R. D. *Acta Crystallogr.* **1976**, *A32*, 751.

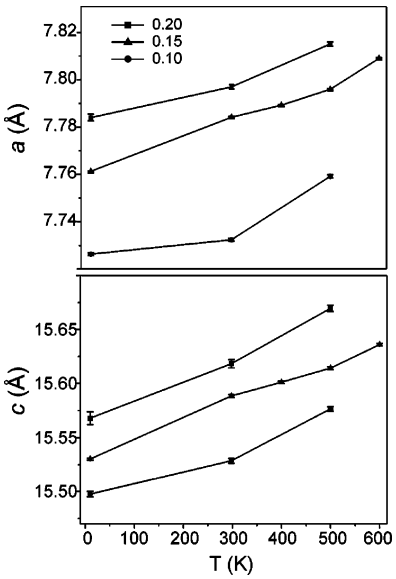

Figure 15. Temperature dependence of the cell parameters of as-prepared $Sr_{1-x}Bi_xCoO_{3-y}$, $x = 0.10$, 0.15, and 0.20.

with increasing Bi content. The cobalt oxidation state decreases from approximately +3.35 for the $x = 0.10$ sample to +3.0 for the $x = 0.20$ phase, and an accompanying increase of the average cobalt ionic size occurs. This expansion is, we believe, the dominant factor governing the cell parameters. It is possible that similar effects are also at work in the $Sr_{1-x}Ln_xCoO_{3-\delta}$ phases for which the expected trend of decreasing cell constants with increasing levels of the smaller Ln^{3+} ions is observed.[8,9] If the oxygen content across a particular Ln series is more or less constant, as claimed by Goossens et al. for $Ho_{1-x}Sr_xCoO_{3-\delta}$, $0.67 \leq x \leq 0.95$,[13] then the observed reduction in cell parameters reflects the increasing amount of lanthanide *despite* a decreasing cobalt oxidation state. This is achievable as the size difference between the A cations, Sr^{2+} and Ln^{3+}, is considerably greater than that between Sr^{2+} and Bi^{3+}.

In contrast to the structural complexity of the as-prepared samples, the oxygen-annealed samples are satisfactorily described as oxygen-deficient cubic perovskites. The neutron analyses for the $x = 0.15$ sample show that some oxygen vacancies remain after oxygen treatment (Table 2). A level of oxygen deficiency is confirmed from the titrations performed on the sample, which give an oxygen content of $O_{2.90(1)}$ and a cobalt valence of +3.65, significantly increased from +3.29 of the as-prepared precursor. The presence of diffuse scattering in the ED patterns (see Figure 9b) indicates that some partial ordering of the remaining oxygen vacancies persists in the samples, although on a length scale significantly reduced from that exhibited by their as-prepared counterparts.

The presence of a large number of oxygen vacancies in the as-prepared $Sr_{1-x}Bi_xCoO_{3-y}$ materials was unsurprising given the behavior of the related $Ln_{1-x}Sr_xCoO_{3-\delta}$ ($0.05 \leq x \leq 0.5$) phases. It was therefore not unexpected that the cubic cell parameters of the compounds determined from the PXD scans showed a significant contraction after oxygen annealing consistent with insertion of oxygen and oxidation of cobalt. Further structural characterization revealed that the oxygen uptake is associated with a phase transition from the *I*4/*mmm* supercell to the $Pm\bar{3}m$ perovskite structure, the tetragonal-to-cubic transition thereby explaining the reduction of peak widths noted for the PXD patterns of the O_2-annealed samples. The TGA and calorimetric traces shown in Figure 10 allow us to follow the phase transition in more detail. Both the $x = 0.10$ and $x = 0.20$ samples show increases in mass prior to the appearance of exothermic peaks in the calorimetric responses. As additional oxygen ions are incorporated into the oxygen-deficient CoO_{4-x} layers, a critical point is reached, at which the number of remaining oxygen vacancies becomes too few for the supercell structure to be supported and the materials transform to the lower energy cubic cell. The exothermic nature of the transition indicates that the supercell structure is metastable. Our understanding is that it is stabilized by quenching the samples to RT. This conclusion is supported by the formation of multiphasic products consisting predominantly of $Sr_6Co_5O_{15}$ obtained when samples were allowed to cool in the furnace. The two-stage oxygen incorporation displayed by $Sr_{0.8}Bi_{0.2}CoO_{3-y}$ (Figure 10b) indicates that a new phase is stabilized in the temperature range 400−600 °C with oxygen content intermediate between those of the as-prepared and cubic phases. Detailed investigations into the full structural implications and the cyclability of the oxidation process for this material are ongoing.

Finally, we note that the $Sr_{1-x}Bi_xCoO_{3-y}$ phases are the first samples in the *I*4/*mmm* supercell series that exhibit such a significant oxygen uptake and associated structural transition. Results of TGA runs under flowing oxygen reported for $Sr_{0.7}Y_{0.3}CoO_{2.62}$ show that the oxygen content is only marginally increased,[5] whereas Maignan et al. used 100 atm of oxygen pressure to insert $\delta = 0.04$ oxygen ions per formula unit into their post-annealed sample of $Sr_{2/3}Y_{1/3}CoO_{2.66+\delta}$.[12] In the final stage of the synthesis of $Ln_{0.33}Sr_{0.67}CoO_{3-\delta}$, Ln = Y, Ho, and Dy, reported by Withers et al.,[4] the samples are heated at 1100 °C under flowing oxygen, suggesting that these phases are also close to their maximum oxygen content. The reason for this apparent anomaly might be the high stability of the *I*4/*mmm* structure for the lanthanide-substituted phases. In particular, it is clear that any uptake of oxygen for the $Ln_{1-x}Sr_xCoO_{3-\delta}$ phases would be accompanied by an energetically unfavorable increase in coordination number for the smaller (in comparison to Bi^{3+}) lanthanide ions.

The as-prepared $Sr_{1-x}Bi_xCoO_{3-y}$ phases adopt the same AFM G-type magnetic structure as exhibited by the $Ln_{1-x}Sr_xCoO_{3-\delta}$ ($x \approx 0.3$, Ln = Y, Dy, Ho) phases,[8,11] suggesting that the magnetic properties of the systems are closely related. However, important differences are apparent from the magnetization data that affect the interpretation of the NPD results. First, we note that all three $Sr_{1-x}Bi_xCoO_{3-y}$ samples display significant magnetic intensity at RT. The temperature dependence of the refined moments is plotted in Figure 16, which shows that the $x = 0.15$ sample has an ordered moment of 1.40(2) μ_B at $T = 400$ K and a presumed value of $T_{Néel}$ close to 450 K. This indicates that the strength of the AFM coupling is greater in the Bi-substituted phases compared with $Y_{0.33}Sr_{0.67}CoO_{2.79}$, for which Goossens et al. reported $T_{Néel} = 320$ K from NPD.[11] In close

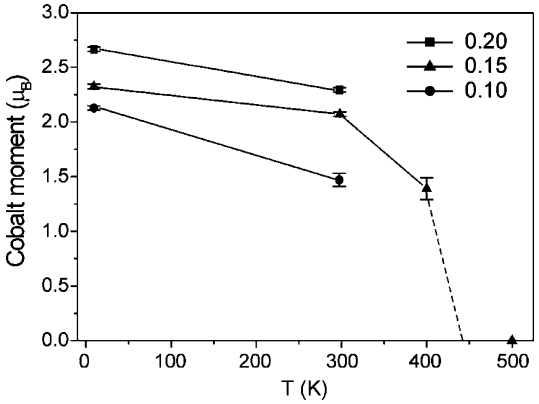

Figure 16. Magnitude of the refined cobalt moments of as-prepared $Sr_{1-x}Bi_xCoO_{3-y}$, $x = 0.10$, 0.15, 0.20.

agreement, Maignan et al. observed a maximum at $T \approx 300$ K in ac-susceptibility measurements for their as-prepared $Y_{0.33}Sr_{0.67}CoO_{2.66}$ sample.[12] The low-temperature moments of 2.14(3), 2.32(2), and 2.64(2) μ_B per cobalt ion obtained for the $Sr_{1-x}Bi_xCoO_{3-y}$ series with increasing x are also greater than the 2.0 ± 0.3 μ_B reported for $Y_{0.33}Sr_{0.67}CoO_{2.79}$. It is now important to recognize that Goossens et al., on the basis of their susceptibility data, suggested that ferromagnetic clusters located in an AFM matrix are present for their $Y_{0.33}Sr_{0.67}CoO_{2.79}$ sample.[11] Consequently, the refined moment reflects only the portion of their phase that is AFM ordered. In contrast, the magnetization results obtained for the $x = 0.15$ as-prepared sample show little or no evidence of ferromagnetism (Figures 11 and 12a), implying that the ground state of the material is antiferromagnetic, an observation consistent with the higher $T_{Néel}$ of the material. Assuming that this dominant AFM nature holds for the $x = 0.10$ and 0.20 samples allows us to speculate on possible spin states based on the observed moments and oxidation states deduced from the titrations. It is important to stress from the outset that the usefulness of such an exercise is limited by the remaining uncertainties associated with the refined moment arising from the effect of covalency and possible unquenched orbital contributions for both Co^{3+} and Co^{4+} ions. In general, the sizes of the moments lie closer to the values expected for an intermediate-spin ($S = 1$) state for the cobalt 3+ ions, in comparison to a high-spin ($S = 2$) state, albeit with a significant orbital contribution necessary for the $x = 0.15$ and 0.20 samples, i.e., 2.0 μ_B is the maximum spin-only moment expected for an $S = 1$ ion. It is also possible to reconcile the moments with the presence of high-spin Co^{3+} ions and low-spin ($S = {}^1/_2$) Co^{4+} ions if considerable covalency and/or disorder is assumed. However, from an application of the Goodenough−Kanomori exchange rules,[28,29] such an arrangement would be expected to yield ferromagnetic coupling for the $x = 0.15$ and 0.10 samples that contain a level of Co^{4+}, in conflict with the magnetization data obtained for the $x = 0.15$ sample. At present, therefore, we favor the presence of intermediate-spin Co^{3+} ions with the e_g electron located in the d_{3z^2} orbital [consistent with the elongated $Co(1)O_6$ coordination] and low-spin Co^{4+} ions to explain the antiferromagnetism of the materials. The trend

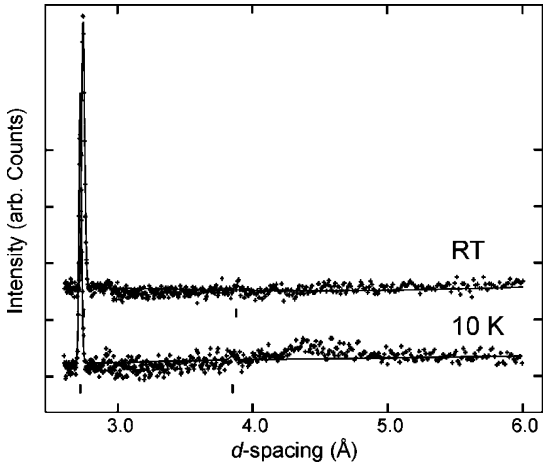

Figure 17. Comparison of the high-d-spacing portion of the NPD patterns obtained for O_2-annealed $Sr_{0.85}Bi_{0.15}CoO_{3-y}$ at RT and 10 K. Intensity in the 4−5 Å range indicates the presence of diffuse magnetic scattering at 10 K.

of increasing moment with increasing Bi content finds a natural explanation as the level of $S = {}^1/_2$, Co^{4+}, reduces across the series regardless of whether the intermediate-spin or high-spin Co^{3+} scenario is in fact the correct picture.

The magnetization results obtained for O_2-annealed $Sr_{0.85}Bi_{0.15}CoO_{3-y}$ show both a large increase in the magnitude of the magnetization in comparison to the as-prepared sample and magnetic irreversibility indicative of spin-glass formation below $T \approx 80$ K. The most compelling explanation for the transformation of the magnetism is the presence of strongly ferromagnetic double exchange between high-spin Co^{3+} and low-spin Co^{4+} ions that competes with antiferromagnetic high-spin (or intermediate-spin) Co^{3+}−Co^{3+} superexchange couplings,[29,30] a hypothesis that implies that a spin state transition accompanies the tetragonal-to-cubic structural transition for at least some of the Co^{3+} ions. Doumerc et al.[30] have shown that the more regular CoO_6 coordination found in the cubic perovskite would be expected to favor a high-spin electronic configuration over an intermediate-spin state for the layered compound $TlSr_2CoO_5$. The $M(H)$ measurements (Figure 12b) reveal that the material does not saturate, not even in fields as large as several tesla, and we cannot therefore draw conclusions concerning possible spin states from these data. The absence of magnetic Bragg reflections in the NPD scans also precludes an estimate of spin state. Closer inspection of the high d-spacing range of the NPD patterns, however, reveals the presence of weak diffuse magnetic scattering in the 10 K data (Figure 17). This observation is consistent with scattering from moments showing some short-range correlation as expected below the freezing temperature of a spin glass. The magnetic feature does not lie on a lattice site of the $Pm\bar{3}m$ structure, suggesting that it is linked to short-range-ordered AFM regions. In fact, the broad peak is centered at $d \approx 4.5$ Å, which coincides with the most intense 112 magnetic reflection observed for the as-prepared phases. It appears, therefore, that small magnetically ordered domains of the AFM superstructure persist in the oxygenated sample, a conclusion in accordance

(28) Goodenough, J. B. *Phys. Rev.* **1955**, *100*, 564.
(29) Kanomori, J. *J. Appl. Phys.* **1960**, *31S*, 14.
(30) Doumerc, J. P.; Coutanceau, M.; Demourgues, A.; Elkaim, E.; Grenier, J. C.; Pouchard, M. *J. Mater. Chem.* **2001**, *11*, 78.

with both the ED results and the strongly AFM nature of the material suggested from the linear dependence of the low-*T*, high-field magnetization curves (Figure 12b). Spin glass formation has been observed for related $Y_{1-x}Sr_xCoO_{3-\delta}$ phases at low doping levels, i.e., $x \leq 0.10$,[10] and the archetypical $La_{1-x}Sr_xCoO_{3-\delta}$ system displays glassy ferromagnetism for $x \leq 0.20$.[31]

In summary, we have demonstrated that the rich structural and magnetic properties of the newly discovered supercell $Sr_{1-x}Ln_xCoO_{3-\delta}$ perovskites are also present in analogous Bi^{3+}-substituted systems. In comparison, the bismuth-containing phases form for lower substitution levels, $x \leq 0.20$, and display a more disordered distribution of oxygen defects in the basal plane of the oxygen-deficient $Co(1)O_{4-x}$ layer. The $Sr_{1-x}Bi_xCoO_{3-y}$ compounds also show the ability to oxidize to form cubic perovskites with reduced oxygen deficiency and increased ferromagnetic nature. Further work on these materials, focusing on a more precise control of oxygen content and its implications for both crystal structure and magnetism, is currently underway.

Acknowledgment. This work was made possible by the provision of an Intra-European Marie Curie Fellowship from the European Commission Sixth Framework Programme to C.S.K. The research was also supported by the Swedish Research Council and the Foundation for Strategic Research (Complex Oxide and FRAM programs) Prof. Mats Nygren is acknowledged for the TGA experiments and for valuable discussions. The authors are also grateful to the Institut Laue Langevin for the provision of neutron beam time, to Dr. Paul Henry for technical assistance during the diffraction experiments, and to Joakim Holmlund for data collection.

CM052457J

(31) Wu, J.; Leigthon, C. *Phys. Rev. B* **2003**, *67*, 174408.